


Article

Effect of Wettability on Collapsing Cavitation Bubble near Solid Surface Studied by Multi-Relaxation-Time Lattice Boltzmann Model

Yipeng Zhu ¹, Minglei Shan ^{1,2,*} , Yu Yang ¹, Qingbang Han ^{1,2}, Changping Zhu ^{1,2} and Xuewu Zhang ^{1,2}

¹ College of Internet of Things Engineering, Hohai University, Changzhou 213022, China; China_czh_zyp@126.com (Y.Z.); kris_yang711@126.com (Y.Y.); Hqb0092@163.com (Q.H.); cpzhu5126081@163.com (C.Z.); Lab_112@126.com (X.Z.)

² Jiangsu Key Laboratory of Power Transmission and Distribution Equipment Technology, Hohai University, Changzhou 213022, China

* Correspondence: shanming2003@126.com; Tel.: +86-135-8457-2036

Received: 12 April 2018; Accepted: 31 May 2018; Published: 6 June 2018



Abstract: The interaction between cavitation bubbles and solid surfaces is an important issue when investigating the mechanism of collapsing cavitation bubbles. The property of a solid surface has a great effect on the inception, development and collapse of the bubbles. In this work, we aim to investigate the effect of wettability on collapsing cavitation bubbles using the multi-relaxation-time lattice Boltzmann model. First, the pseudopotential multi-relaxation-time lattice Boltzmann is improved by involving the piecewise linear equation of state and the improved forcing scheme modified by Li et al. The improved pseudopotential model is verified by the Laplace law. Next, the fluid–solid interaction in the model is employed to adjust the wettability of the solid surface. Moreover, the simulation of the collapse of the cavitation bubble near the solid surface is compared by the experiment results. Finally, the simulation of the collapsing cavitation bubbles near the solid surface with different wettability is also investigated. We find that the numerical results of the collapsing bubble are in good agreement with the experimental results. The simulation results show that the hydrophobicity of the solid surface can accelerate the cavitation bubble collapse. The hydrophilicity of the solid surface has little effect on the collapsing bubbles.

Keywords: cavitation bubble; wettability; lattice Boltzmann model; pseudopotential model

1. Introduction

Cavitation is a unique physical phenomenon occurring in a liquid, which is a perpetual research subject due to its specific dynamic effects [1–3]. Collapsing cavitation bubbles usually produce extreme physical phenomena, such as high velocities, high pressures and high temperature in partial areas. While a collapsing cavitation bubble is close to a solid surface, these physical phenomena cause serious damage to the surface of the material, which is called cavitation erosion. On the other hand, collapsing cavitation bubbles have been widely used in various applications, such as material surface modifications [4–6] and medical fields [7–9]. From these applications, we can extract a valuable and general issue, i.e., the investigation of the interaction between cavitation bubbles and a solid surface with different properties.

Many research papers have discussed the interaction between a surface and a cavitation bubble from different perspectives, including the roughness of the surface, interfacial wettability, and surface tension. With their experiments, Li et al. studied the effects of nozzle inner surface roughness on the cavitation erosion characteristics of high-speed submerged jets [10]. Their findings showed that

geometric characteristics of the surface have great effects on cavitation erosion intensity at standoff distances around or exceeding the optimum. Belova et al. explored the controlled effect of ultrasonic cavitation on hydrophobic/hydrophilic surfaces [11]. They developed a selective control scheme of ultrasonic cavitation on metal surfaces with different hydrophobicities. Their findings from the experiments showed that cavitation prefers to dominate on hydrophobic surfaces due to the low nucleation barrier. Due to the limitations of the experiment, the microcosmic mechanism of interaction between the cavitation bubble and the solid surface was not discussed in their work.

The lattice Boltzmann method (LBM), as a mesoscopic approach based on the kinetic Boltzmann equation, has been rapidly developed in recent years [12]. LBM has been employed in research on the interaction between the cavitation and surface of solid surface materials due to its convenience in multiphase and fluid–solid surface modeling [13]. In References [13], Ezzatneshan discussed the effects of wettability on cavitation inception using LBM. The study showed that the pseudopotential LBM was robust and efficient for predicting cavitation phenomena with surface wettability effects considered. It was also accurate enough for cavitation flow under different conditions. However, the above researchers' works do not involve the stage of the collapsing cavitation bubble, which is critical for the interaction between cavitation and the solid surface.

The challenge of the simulation of the collapsing cavitation bubble near the solid surface is the stability of the lattice Boltzmann (LB) model. For the pseudopotential multiphase model [14], the stability is closely related to the thermodynamic consistency, and many efforts have been made for this issue [15–17]. Recently, Shan et al. [18] studied the evolution of the collapsing cavitation bubble near a rigid boundary using LBM. They established a collapsing bubble model using an improved forcing scheme based on that of Li et al. [16]. The numerical results were compared with experimental results. Shan's research demonstrated that the pseudopotential multi-relaxation-time (MRT) LB could successfully simulate the collapsing cavitation bubble near the solid wall. However, there is no fluid–solid interaction added in the simulation model.

In the present work, the pseudopotential MRT LB with the improved forcing scheme proposed by Li Q et al. [17,19,20] is applied to investigate the cavitation bubble collapse near the hydrophobic or hydrophilic surface. The fluid–solid interaction is adapted to the pseudopotential MRT LB to achieve the fluid–solid boundary. The simulation using LBM was validated through the comparison between the numerical results and experimental results. The effect of hydrophilicity and hydrophobicity on the inception and the collapsing cavitation bubble is also discussed.

2. Pseudopotential MRT LB Model

The pseudopotential LB model with MRT operation collision was employed in the present work [21,22]. The evolution equation can be given as [23]:

$$f_{\alpha}(\mathbf{x} + \mathbf{e}_{\alpha}\delta_t, t + \delta_t) = f_{\alpha}(\mathbf{x}, t) - (\mathbf{M}^{-1}\mathbf{\Lambda}\mathbf{M})_{\alpha\beta} (f_{\beta} - f_{\beta}^{eq}) + \delta_t F'_{\alpha} \quad (1)$$

where f_{α} denotes the density distribution function, f_{α}^{eq} is its equilibrium distribution, t is the time, \mathbf{x} denotes the spatial position, \mathbf{e}_{α} is the discrete velocity along the α th direction, δ_t is the time step, F'_{α} is the component of forcing term F' in the velocity space, \mathbf{M} is an orthogonal transformation matrix, and $\mathbf{\Lambda}$ is a diagonal matrix given by (for the D2Q9 lattice) [24]

$$\mathbf{\Lambda} = \text{diag}(\tau_{\rho}^{-1}, \tau_e^{-1}, \tau_{\xi}^{-1}, \tau_j^{-1}, \tau_q^{-1}, \tau_j^{-1}, \tau_q^{-1}, \tau_v^{-1}, \tau_v^{-1}) \quad (2)$$

The τ_{ρ}^{-1} , τ_e^{-1} , τ_{ξ}^{-1} , τ_j^{-1} , τ_q^{-1} and τ_v^{-1} is related to density, energy, energy squared, components of momentum flux, energy flux components and stress tensor. These relaxation times were chosen as $\tau_v = \tau_{\rho} = \tau_j = 1.0$, $\tau_e^{-1} = \tau_{\xi}^{-1} = 0.8$ and $\tau_q^{-1} = 1.1$ in this paper. Through the transformation matrix

\mathbf{M} [25], the f_α and f_α^{eq} can be projected onto the moment space via $\mathbf{m} = \mathbf{M}\mathbf{f}$ and $\mathbf{m}^{eq} = \mathbf{M}\mathbf{f}^{eq}$. Thus, the collision step of Equation (1) can be rewritten as:

$$\mathbf{m}^* = \mathbf{m} - \Lambda(\mathbf{m} - \mathbf{m}^{eq}) + \delta_t \left(\mathbf{I} - \frac{\Lambda}{2} \right) \mathbf{S} \quad (3)$$

where the \mathbf{I} is the unite tensor, and the \mathbf{S} is the forcing term in the moment space with $(\mathbf{I} - 0.5\Lambda)\mathbf{S} = \mathbf{M}\mathbf{F}$. In D2Q9 lattice, \mathbf{m}^{eq} can be given by [20]:

$$\mathbf{m}^{eq} = \rho \left(1, -2 + 3|\mathbf{v}|^2, 1 - 3|\mathbf{v}|^2, v_x, -v_x, v_y, -v_y, v_x^2 - v_y^2, v_x v_y \right)^T \quad (4)$$

where the $\rho = \sum_\alpha f_\alpha$ is the macroscopic density, \mathbf{v} is the macroscopic velocity calculated by:

$$\mathbf{v} = \left(\sum_\alpha \mathbf{e}_\alpha f_\alpha + \frac{\delta_t}{2} \mathbf{F} \right) / \rho \quad (5)$$

Here, $\mathbf{F} = (F_x, F_y)$ is the total force acting on the system for two-dimensional (2D) space and $|\mathbf{v}|^2 = v_x^2 + v_y^2$. Then the streaming step of the MRT LB equation can be formulated as:

$$f_\alpha(\mathbf{x} + \mathbf{e}_\alpha \delta_t, t + \delta_t) = f_\alpha^*(\mathbf{x}, t) \quad (6)$$

where $\mathbf{f}^* = \mathbf{M}^{-1} \mathbf{m}^*$.

In the pseudopotential LB model, the intermolecular interaction force is defined via a pseudopotential ψ , which depends on the local density. It is given as [26]:

$$\mathbf{F}_m = -G\psi(x) \sum_\alpha w_\alpha \psi(\mathbf{x} + \mathbf{e}_\alpha) \mathbf{e}_\alpha \quad (7)$$

where G is the interaction strength, and w_α is the weight. The weight $w_\alpha = 1/3$ for $|\mathbf{e}_\alpha|^2 = 1$ and the weight $w_\alpha = 1/12$ for $|\mathbf{e}_\alpha|^2 = 2$ on D2Q9 lattice for the nearest-neighbor interactions.

According to Yuan and Schaefer [27], the pseudopotential ψ is taken as:

$$\psi = \sqrt{2(p_{EOS} - \rho c_s^2) / Gc^2} \quad (8)$$

in which p_{EOS} represents a prescribed equation of state. The parameter G is set as $G = -1$ to ensure the whole term is inside the square root positive. The parameter c is the lattice constant, and $c_s = c/\sqrt{3}$ is the lattice sound speed. The piecewise linear equation of state (EOS) proposed by Colosqui et al. [28] is applied in the model and is given by:

$$p(\rho) = \begin{cases} \rho\theta_v & \text{if } \rho < \rho_1 \\ \rho_1\theta_v + (\rho - \rho_1)\theta_m & \text{if } \rho_1 < \rho < \rho_2 \\ \rho_1\theta_v + (\rho_2 - \rho_1)\theta_m + (\rho - \rho_2)\theta_l & \text{if } \rho > \rho_2 \end{cases} \quad (9)$$

where $\theta_v = \sqrt{(\partial p / \partial \rho)_v}$ and $\theta_l = \sqrt{(\partial p / \partial \rho)_l}$ represent the speeds of sound the vapor phase and liquid phase, respectively; θ_m is the slope in the unstable branch ($\partial p / \partial \rho < 0$). The variables ρ_1 and ρ_2 can be obtained by solving a set of two equations. One equation is ensured for mechanical equilibrium:

$$\int_{\rho_v}^{\rho_l} dp = (\rho_1 - \rho_v)\theta_v + (\rho_2 - \rho_1)\theta_m + (\rho_l - \rho_2)\theta_l = 0 \quad (10)$$

and the other is ensured for chemical equilibrium:

$$\int_{\rho_v}^{\rho_l} \frac{1}{\rho} d\rho = \log\left(\frac{\rho_l}{\rho_v}\right)\theta_v + \log\left(\frac{\rho_m}{\rho_l}\right)\theta_m + \log\left(\frac{\rho_l}{\rho_m}\right)\theta_l = 0 \quad (11)$$

where ρ_l and ρ_v represent the density of vapor and liquid, respectively.

With the pseudopotential ψ , the pseudopotential LB model usually undergoes thermodynamic inconsistency. Subsequently, Li et al. [20] found that the thermodynamic consistency can be approximately achieved by adjusting the mechanical stability condition via an improved forcing scheme [17]

$$\mathbf{S} = \begin{bmatrix} 0 \\ 6\mathbf{v} \cdot \mathbf{F} + \frac{12\sigma|\mathbf{F}_m|^2}{\psi^2\delta_t(\tau_e-0.5)} \\ -6\mathbf{v} \cdot \mathbf{F} - \frac{12\sigma|\mathbf{F}_m|^2}{\psi^2\delta_t(\tau_e-0.5)} \\ F_x \\ -F_x \\ F_y \\ -F_y \\ 2(v_x F_x - v_y F_y) \\ v_x F_y + v_y F_x \end{bmatrix} \quad (12)$$

where $|\mathbf{F}_m|^2 = (F_{m,x}^2 + F_{m,y}^2)$. The parameter \mathbf{F}_m in Equation (12) denotes the intermolecular interaction force, and \mathbf{F} is the total force of the system; and σ is used to tune the mechanical stability condition. In this work, from the investigation of the thermodynamic consistency [20,24], σ is set as 0.11625 in the case of cavitation bubble and 0.084 in the case of a droplet on the surface, respectively.

The adhesive force at the solid surface should be considered in the pseudopotential MRT LB model. The wettability of a solid surface is decided by the adhesive force in the model. The following fluid–solid interaction [29] to mimic the adhesive force is given by:

$$\mathbf{F}_{ads} = -G_w \rho(\mathbf{x}) \sum_{\alpha} \omega_{\alpha} S(\mathbf{x} + \mathbf{e}_{\alpha}) \mathbf{e}_{\alpha} \quad (13)$$

where G_w is the adsorption parameter, $\omega_{\alpha} = c_s^2 w_{\alpha}$ and the switch function $S(\mathbf{x} + \mathbf{e}_{\alpha})$ is $\psi(\mathbf{x})s(\mathbf{x} + \mathbf{e}_{\alpha})$ which is equal to 1 or 0 for a solid or a fluid phase, respectively. The total force in Equation (12) is given by $\mathbf{F} = \mathbf{F}_m + \mathbf{F}_{ads}$.

In this paper, the lattice units for LB are adopted. The basic units of length, time and mass are lu (lattice unit), ts (time step) and mu (mass unit), respectively. Thus, the units of velocity, pressure, and density are expressed as lu/ts , $mu/(ts^2 lu)$ and mu/ts^2 , respectively.

3. Numerical Simulation and Analysis

3.1. Laplace Law and the Contact Angle

Laplace law is the validation of the multi-phase model. For the case of the cavitation bubble, the Laplace law can be given as:

$$\Delta p = p_{in} - p_{out} = \frac{\gamma}{R_0}, \quad (14)$$

where the p_{in} and p_{out} are the pressures inside and outside of the bubble, respectively. R_0 is the radius of the bubble, γ is the surface tension. The computational domain is 700×700 lattice system.

The periodic boundary condition is applied in two directions of the boundary. The density field is initialized as [18]:

$$\rho(x, y) = \frac{\rho_l + \rho_v}{2} + \frac{\rho_l - \rho_v}{2} \times \tanh \left[\frac{2 \left(\sqrt{(x - x_0)^2 + (y - y_0)^2} - R_0 \right)}{W} \right], \quad (15)$$

where W is the prescribed width of the phase interface and it is 5 in the present work; ' \tanh ' is a hyperbolic tangent function and it is set as $\tanh(x) = (e^{2x} - 1) / (e^{2x} + 1)$.

To mimic the experimental value, the density ratio is set as 500 with $\rho_l = 500$ and $\rho_v = 1$. The other parameters including $\rho_1, \rho_2, \theta_v, \theta_m$ and θ_l are set as 1.36, 481.04, 0.2133, -0.01333 and 0.33333, respectively. The lattice constant c and the time step δ_t are both set as 1. The bubble is placed at the center of the computational domain. The radius R_0 is set as 60, 65, 70, 75 and 80, respectively.

Figure 1 shows the linear relationship between the Δp and $1/R_0$. It indicates that the simulation results agree well with Young-Laplace law and verify the improved pseudopotential MRT LB model.

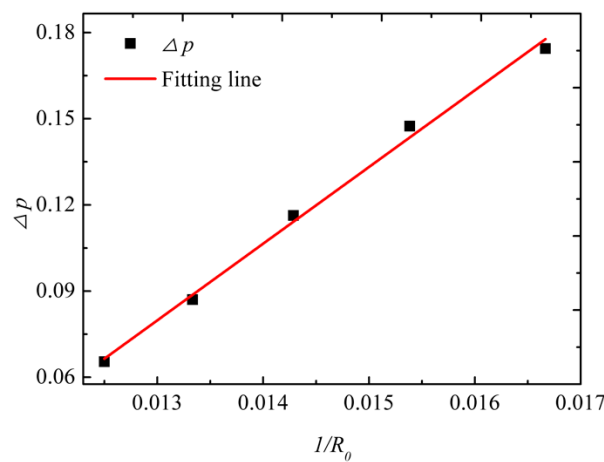


Figure 1. The validation of Young-Laplace law.

In this paper, the wettability of the surface was measured by the achievable contact angle. It is a general practice that wettability is obtained by measuring the contact angle of a droplet on the solid surface. The contact angle $\theta > 90^\circ$ means the surface is hydrophobic and $\theta < 90^\circ$ means the surface is hydrophilic. In the computational domain, the 400×400 lattice system was adopted in our simulations. The open boundary condition was employed at the top boundary. The nonslip boundary scheme [30] was applied at the bottom boundary $f_5 = f_7 - 0.5(f_1 - f_3) - 0.25\delta_t(F_x + F_y)$, $f_6 = f_8 + 0.5(f_1 - f_3) + 0.25\delta_t(F_x + F_y)$ and $f_2 = f_4$. The density field was initialized as [17]

$$\rho(x, y) = \frac{\rho_l + \rho_v}{2} - \frac{\rho_l - \rho_v}{2} \times \tanh \left[\frac{2 \left(\sqrt{(x - x_l)^2 + (y - y_l)^2} - R_l \right)}{W} \right], \quad (16)$$

where (x_l, y_l) is the center of the droplet and is (200, 40).

The parameter R_l which represents the radius of the droplet is initialized as 40. The initial density ratio is 500 with $\rho_l = 500$ and $\rho_v = 1$.

In the simulations, the intermolecular interaction force and the fluid-solid interaction force are used at the solid surface. Consequently, a contact angle of $\theta = 90^\circ$ can be analytically achieved when G_w is 0 which represents the neutral wettability. The results of contact angles corresponding to different G_w are shown in Figure 2. The obtained contact angle θ is 91.5° when G_w is set as 0. This

means that the numerical result was in good agreement with the analytical solution. As is shown in the results, the contact angle was approximately proportional to the parameter G_w . It may be said that the wettability of the solid surface can be adjusted by G_w in the simulation.

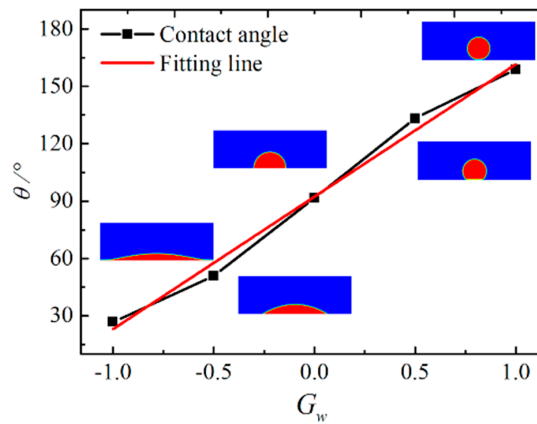


Figure 2. The contact angle with different G_w (hydrophobicity: contact angle $\theta > 90^\circ$, hydrophilicity: contact angle $\theta < 90^\circ$).

3.2. Verification of the Collapsing Bubble Near the Solid Surface

In this section, the pseudopotential MRT LB with the fluid–solid interaction is used to investigate the collapsing bubble near the solid surface. The simulations are verified compared with the experimental results.

In present work, the computational domain for the collapsing bubble near the solid surface is established in 700×700 lattice system which is shown in Figure 3. The open condition [31] is applied in the top boundary and the periodic boundary conditions are employed in a vertical direction. The bottom boundary uses the nonslip boundary scheme. The density field is the same as that in the Equation (16). In Figure 3, R_0 represents the radius of the bubble and b_0 denotes the distance between the center of the bubble and the solid surface. The dimensionless position offset parameter $\lambda_0 = R_0/b_0$ which represents the ratio of the radius to the distance between the bubble and the solid surface, was adopted to compare the dynamic process of cavitation bubbles collapsing near the solid surface in different cases [32]. The parameters p_∞ and p_v represent the ambient pressure and the vapor pressure in the bubble, respectively.

In the simulation, the initial R_0 and λ_0 were 80 and 1.3, respectively. The constant pressure difference $\Delta p = p_\infty - p_v$ was 18.334 to ensure the bubble collapse. The density ratio was 500 with $\rho_l = 500$ and $\rho_v = 1$. The parameter G_w in fluid–solid interaction was 0 for this case [33].

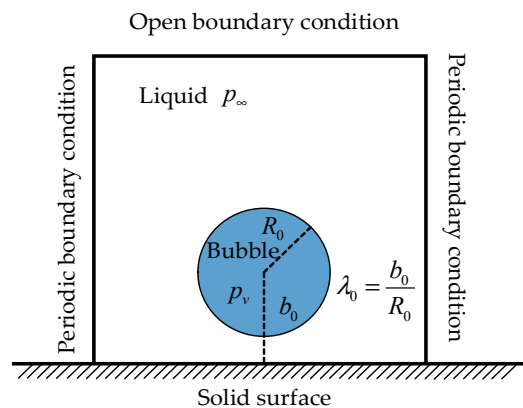


Figure 3. The computational domain for the collapsing bubble near the solid surface.

Figure 4 shows a comparison between the numerical and experimental results. It is clearly shown that the numerical results were in good agreement with the experiment. The spherical bubble shrank from the top pressure in the initial state. As time passes, the sunken region of the bubble grows, and, in the final stage, the jet of the bubble will form when the bubble is collapsing.

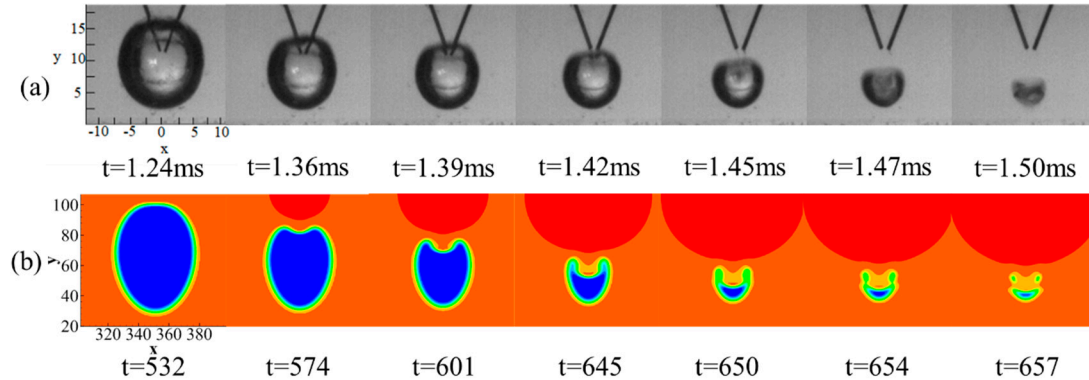


Figure 4. The comparison about evolutions of the bubble between numerical and the experimental results ((a) experimental results: $\lambda_0 \approx 1.3$, $R_0 = 2.50\text{ mm}$; (b) LBM simulation: $\lambda_0 = 1.3$, $R_0 = 80$, $\Delta p = 18.334$).

3.3. Effect of Wettability on Cavitation Inception

The effect of wettability of the surface on the cavitation inception is investigated by changing wettability with setting the negative pressure in the liquid domain. The parameters of the EOS are the same as the parameters in Section 3.1. The cavitation inception is produced by setting the negative pressure at the computational domain. The negative pressure is used to simulate the conditions of cavitation such as the process of an internal tear. The negative pressure can be acquired by reducing the initial density of the equilibrium state. Subsequently, the paper discusses the time of cavitation generation under different negative pressure conditions. Thus, the paper studies these cases where the negative pressure is set as -6.02 , -5.69 , -5.36 , -5.02 , -4.69 and -4.36 , respectively.

The simulation results about the effect of the hydrophobicity on the cavitation inception are shown in Figure 5. It shows that the time of cavitation inception is short with the enhancement of the hydrophobicity of the surface. It means the hydrophobicity can accelerate the cavitation inception. There is no cavitation inception when the surface is hydrophilic in our simulation results. These simulation results verify the conclusion of Reference [11] from the perspective of numerical analysis.

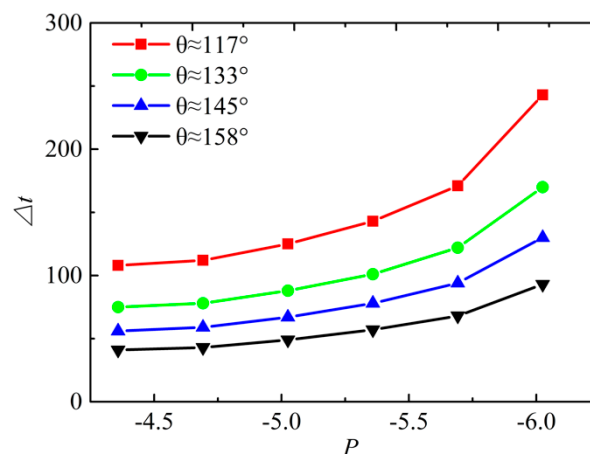


Figure 5. The effect of the hydrophobicity on the cavitation inception.

4. The Effect of Wettability on the Collapsing Bubble near the Solid Surface

In this section, the effect of wettability on the collapsing bubble near the solid surface may be studied by comparing the shape of the bubble and collapsing time. The parameter λ_0 in Figure 3 is set as 1.0, 1.1 and 1.2, respectively to study the bubble near the solid surface. The contact angle θ of the hydrophobic and hydrophilic surfaces is set as 26.87° , 50.93° , 91.50° , 133.32° and 158.84° , respectively. The other parameters are the same as those described in Section 3.2.

The discussion about the results of the simulation is divided into three parts. In the first part, we investigate the density evolution of the collapsing cavitation bubble. Secondly, the time of the collapsing cavitation bubble with different wettability is compared. Finally, the effect of wettability on the density, pressure and velocity distribution of the collapsing bubble near the solid surface is discussed.

Figure 6 shows the density evolution of the collapsing cavitation bubble with the parameter λ_0 set as 1.0. Each row represents the every wettability of the solid surface. The evolution of the collapsing cavitation bubble includes the density distribution when the time steps are 500 and 600. The density distribution of the collapsing bubble is also included in the evolution.

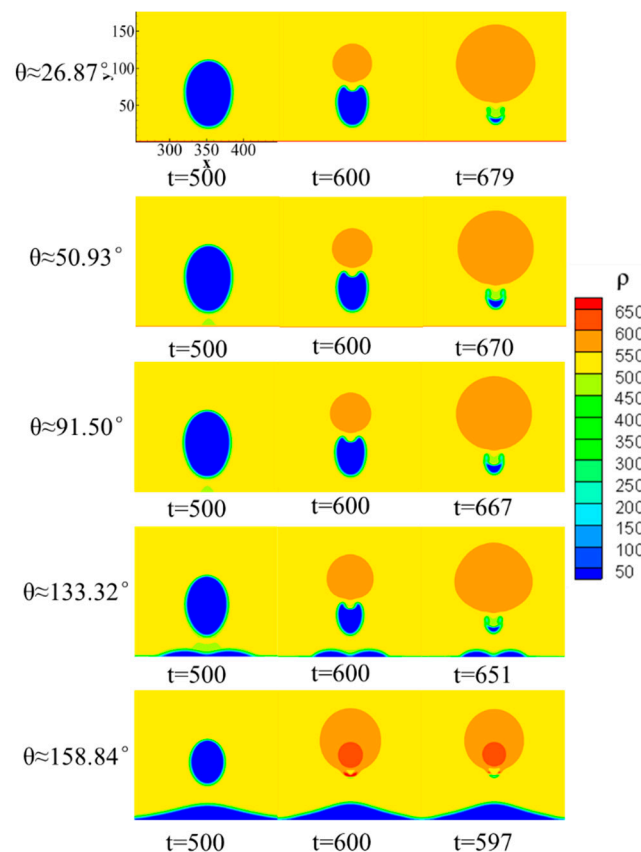


Figure 6. The density evolution of the collapsing cavitation bubble with $\lambda_0 = 1.0$.

In Figure 6, the cavitation bubble sticking to the surface collapses from the pie shape to the bowl shape. There was a high-density region on the bubble. We found that the profile evolutions of cavitation bubbles were almost identical under different hydrophobicities—that is, hydrophobicity almost does not affect the collapsing process of cavitation bubbles. However, there are some changes when the wettability of the surface is hydrophobic. With the increase of the hydrophobicity, the bottom of the cavitation bubble spreads at the surface in a wider range. In the same time step, the size of the cavitation bubble became smaller when the hydrophobicity was stronger. It also means the hydrophobicity accelerated the evolution of the cavitation bubble compared to hydrophilicity. The solid

surface had a retarded effect in the fluid system, which was similar to the Poisson flow effect. When the cavitation bubbles collapsed (volume reduction), the fluid flow and velocity in the direction of the solid surface and the fluid area above the bubbles are different, respectively. Then asymmetry occurs.

The collapsing time of the cavitation bubble is shown in Figure 7. The hydrophobic solid surface obviously affected the collapsing time of the cavitation bubble. With the hydrophobicity being stronger, the collapsing time was shorter. Compared to hydrophobicity, hydrophilicity had little effect on the collapsing time. The collapsing time was shorter when the parameter λ_0 was larger.

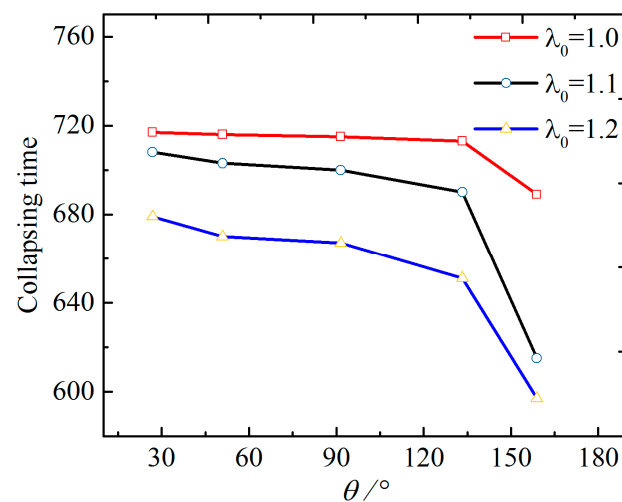


Figure 7. Collapsing time with a different contact angle.

Figure 8 shows the density and pressure distribution of the collapsing cavitation bubble. The left part of the small graph represents the density distribution and the right part represents the pressure distribution (Figure 8). Each column represents the different wettabilities, and each row represents the collapsing cavitation bubble near the solid surface with different λ_0 .

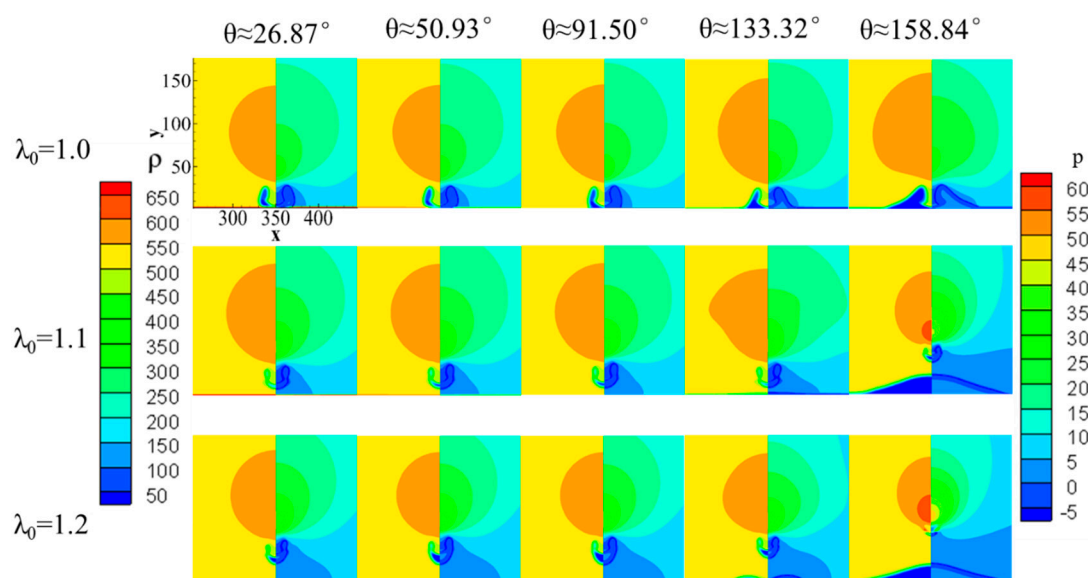


Figure 8. The density and pressure distribution of the collapsing cavitation bubble.

Firstly, unlike the bubble adhesive on the surface, the collapsing cavitation bubble near the solid surface becomes small in size. The high-density region above the bubble becomes small, but the value

of the region becomes high when the hydrophobicity of the surface increases. Another phenomenon is that there are some new arch-like cavitation bubbles generated adhesively to the solid surface when the wettability of the surface is hydrophobicity. The farther the bubble is away from the solid surface, the more obvious these phenomena are.

Secondly, the evolution of pressure is similar to the process of the density distribution. The high-pressure area is distributed in the upper part of the picture, and the low pressure is in the lower part. With the hydrophobicity of the solid surface enhanced, the low-pressure region around the bubble expands, and the high-pressure region is reduced as shown in Figure 8. The pressure of the high-pressure region with strong hydrophobicity is higher than that with strong hydrophilicity. The hydrophilicity has little effect on the cavitation bubble. The phenomenon is visible as the parameter λ_0 is increasing.

To investigate the impact of the jet center on the solid surface and the rules of the velocity changes in numerical value aspect, we used the presentation of the velocity in Figure 9 and it shows the velocity of perpendicular bisector of x-axis in y-direction with the parameter λ_0 set as 1.0, 1.1 and 1.2. The velocity increased first, then dropped to the valley and finally came to a steady value. As the parameter increased, the phenomenon was obvious. The hydrophilicity of surface had a minimal effect on the velocity. However, when the hydrophobicity increases, the peak of the velocity becomes higher and the valley becomes lower. It also meant that the peak represented the edge between the new arch-like bubbles and the liquid. The valley represented the collapsing cavitation bubble.

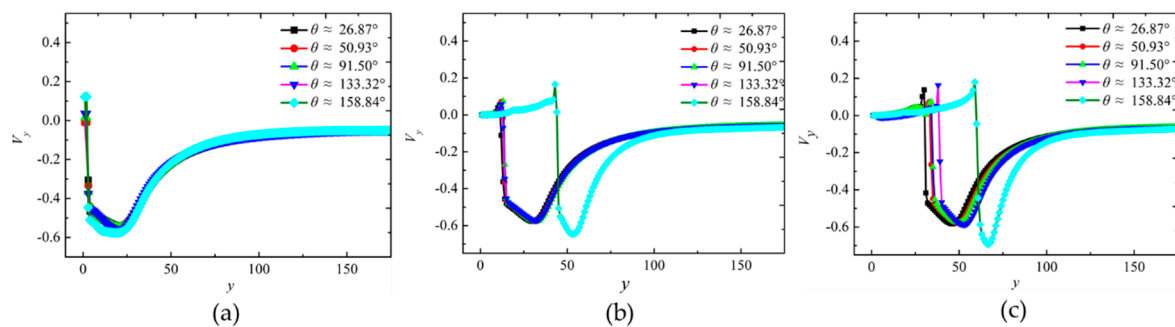


Figure 9. The velocity of the perpendicular bisector of x axis in y direction ((a) $\lambda_0 = 1.0$, (b) $\lambda_0 = 1.1$, (c) $\lambda_0 = 1.2$).

These phenomena can explain the difference between wettability of the surface and the intermolecular interaction force. Particularly, the change from hydrophilicity to hydrophobicity of the solid surface was adjusted by the parameter G_w from -1.0 to 1.0 in the fluid–solid interaction in the model. When the parameter G_w is less than zero, this means the property of the solid surface is hydrophilic. The parameter G in Equation (7) was set as -1 . Thus, the total force F at the bottom boundary was the superposition of the intermolecular interaction force and fluid–solid interaction force. After multiple iterations, the density and pressure at the bottom boundary become higher. However, when the property of the solid surface is hydrophobic, the parameter G_w is greater than zero. The total force F at the bottom boundary is the counteraction of the intermolecular interaction force and fluid–solid interaction force. After multi-iterations, the density and pressure at the bottom boundary become lower.

In general, the hydrophobicity accelerates the evolution of the cavitation bubble while the hydrophilicity has minimal effect on the bubble. In the evolution of the collapsing bubble, the new arch-like cavitation bubble is generated near the solid surface when the wettability of the surface is hydrophobic.

5. Conclusions

In this paper, the pseudopotential multi-relaxation-time lattice Boltzmann model is used to study the wettability on the collapse of the cavitation bubble. The bubble profile in the simulation is in good agreement with the experimental results. The wettability of solid surface can be adjusted by changing the parameter G_w in the fluid-solid interaction force. The results of collapsing bubbles are shown with different hydrophobicity and hydrophilicity of the solid surface. The hydrophobicity of the solid surface can accelerate the cavitation bubble collapsing. However, the hydrophilicity of the solid surface has minimal effect on the cavitation bubble. It results from a difference between wettability of the surface and the intermolecular interaction force. The new arch-like bubble can be generated close to the solid surface when the property of the solid surface is hydrophobic. Our work demonstrates that LBM is an effective tool to simulate a cavitation bubble near different hydrophobicities and hydrophilicities of a solid surface. The influence from the hydrophobicity of a solid surface can provide some insight for the engineering of bubble collapsing applications.

Author Contributions: Y.Z.: literature search, data collection, writing. M.S.: study design, data analysis, literature search. Y.Y.: figures, data collection. Q.H.: literature search, data analysis. C.Z.: data interpretation. X.Z.: data interpretation.

Funding: This work is supported by the National Natural Science Foundation of China (Grant No. 11574072), the National Key Research and Development Program of China (Grant No. 2016YFC0401600), the Primary Research and Development Plan of Jiangsu Province, China (Grant No. BE2016056) and the Fundamental Research Funds for the Central Universities (Grant No. 2017B17814).

Conflicts of Interest: The authors declare no conflicts of interest.

References

1. Bagal, M.V.; Gogate, P.R. Wastewater treatment using hybrid treatment schemes based on cavitation and Fenton chemistry: A review. *Ultrason. Sonochem.* **2014**, *21*, 1–14. [[CrossRef](#)] [[PubMed](#)]
2. Teran Hilares, R.; Ramos, L.; da Silva, S.S.; Dragone, G.; Mussatto, S.I.; Santos, J.C.D. Hydrodynamic cavitation as a strategy to enhance the efficiency of lignocellulosic biomass pretreatment. *Crit. Rev. Biotechnol.* **2017**, *38*, 483–493. [[CrossRef](#)]
3. Kerboua, K.; Hamdaoui, O. Influence of reactions heats on variation of radius, temperature, pressure and chemical species amounts within a single acoustic cavitation bubble. *Ultrason. Sonochem.* **2018**, *41*, 449–457. [[CrossRef](#)]
4. Vyas, N.; Pecheva, E.; Dehghani, H.; Sammons, R.L.; Wang, Q.X.; Leppinen, D.M.; Walmsley, A.D. High Speed Imaging of Cavitation around Dental Ultrasonic Scaler Tips. *PLoS ONE* **2016**, *11*, e0149804. [[CrossRef](#)] [[PubMed](#)]
5. Vyas, N.; Dehghani, H.; Sammons, R.L.; Wang, Q.X.; Leppinen, D.M.; Walmsley, A.D. Imaging and analysis of individual cavitation microbubbles around dental ultrasonic scalers. *Ultrasonics* **2017**, *81*, 66–72. [[CrossRef](#)] [[PubMed](#)]
6. Ye, L.; Zhu, X. Analysis of the effect of impact of near-wall acoustic bubble collapse micro-jet on Al 1060. *Ultrason. Sonochem.* **2017**, *36*, 507–516. [[CrossRef](#)] [[PubMed](#)]
7. Fu, H.; Comer, J.; Cai, W.; Chipot, C. Sonoporation at Small and Large Length Scales: Effect of Cavitation Bubble Collapse on Membranes. *J. Phys. Chem. Lett.* **2015**, *6*, 413–418. [[CrossRef](#)] [[PubMed](#)]
8. Adhikari, U.; Goliaei, A.; Berkowitz, M.L. Nanobubbles, cavitation, shock waves and traumatic brain injury. *Phys. Chem. Chem. Phys.* **2016**, *18*, 32638–32652. [[CrossRef](#)] [[PubMed](#)]
9. Landhuis, E. Ultrasound for the brain. *Nature* **2017**, *551*, 257–259. [[CrossRef](#)] [[PubMed](#)]
10. Li, D.; Kang, Y.; Wang, X.; Ding, X.; Fang, Z. Effects of nozzle inner surface roughness on the cavitation erosion characteristics of high speed submerged jets. *Exp. Therm. Fluid Sci.* **2016**, *74*, 444–452. [[CrossRef](#)]
11. Belova, V.; Gorin, D.A.; Shchukin, D.G.; Mohwald, H. Controlled effect of ultrasonic cavitation on hydrophobic/hydrophilic surfaces. *ACS Appl. Mater. Interfaces* **2011**, *3*, 417–425. [[CrossRef](#)] [[PubMed](#)]
12. Guo, Z.L.; Shu, C. *Lattice Boltzmann Method and Its Applications in Engineering*; World Scientific Publishing: Singapore, 2013; pp. 1–34. ISBN 978-981-4508-29-2.

13. Ezzatneshan, E. Study of surface wettability effect on cavitation inception by implementation of the lattice Boltzmann method. *Phys. Fluids* **2017**, *29*, 113–304. [[CrossRef](#)]
14. Li, Q.; Luo, K.H. Thermodynamic consistency of the pseudopotential lattice Boltzmann model for simulating liquid–vapor flows. *Appl. Therm. Eng.* **2014**, *72*, 56–61. [[CrossRef](#)]
15. Kupershtokh, A.L.; Medvedev, D.A.; Karpov, D.I. On equations of state in a lattice Boltzmann method. *Comput. Math. Appl.* **2009**, *58*, 965–974. [[CrossRef](#)]
16. Li, Q.; Luo, K.H.; Li, X.J. Forcing scheme in pseudopotential lattice Boltzmann model for multiphase flows. *Phys. Rev. E Stat. Nonlinear Soft Matter Phys.* **2012**, *86*, 1–28. [[CrossRef](#)] [[PubMed](#)]
17. Li, Q.; Luo, K.H.; Li, X.J. Lattice Boltzmann modeling of multiphase flows at large density ratio with an improved pseudopotential model. *Phys. Rev. E Stat. Nonlinear Soft Matter Phys.* **2013**, *87*, 1–11. [[CrossRef](#)] [[PubMed](#)]
18. Shan, M.L.; Zhu, C.P.; Zhou, X.; Yin, C.; Han, Q.B. Investigation of cavitation bubble collapse near rigid boundary by lattice Boltzmann method. *J. Hydrodyn. Ser. B* **2016**, *28*, 442–450. [[CrossRef](#)]
19. Li, Q.; Luo, K.H. Achieving tunable surface tension in the pseudopotential lattice Boltzmann modeling of multiphase flows. *Phys. Rev. E Stat. Nonlinear Soft Matter Phys.* **2013**, *88*, 05330701–05330710. [[CrossRef](#)] [[PubMed](#)]
20. Li, Q.; Luo, K.H.; Kang, Q.J.; Chen, Q. Contact angles in the pseudopotential lattice Boltzmann modeling of wetting. *Phys. Rev. E Stat. Nonlinear Soft Matter Phys.* **2014**, *90*, 05330101–05330109. [[CrossRef](#)] [[PubMed](#)]
21. Shan, X.; Chen, H. Lattice Boltzmann model for simulating flows with multiple phases and components. *Phys. Rev. E* **1993**, *47*, 1815–1819. [[CrossRef](#)]
22. Shan, X.; Chen, H. Simulation of nonideal gases and liquid–gas phase transitions by the lattice Boltzmann equation. *Phys. Rev. E* **1994**, *49*, 2941–2948. [[CrossRef](#)]
23. Weaver, D.P.; Shizgal, B.D. *Rarefied Gas Dynamics: Theory and Simulations*; The American Institute of Aeronautics and Astronautics: Reston, VA, USA, 1994; pp. 409–503.
24. Shan, M.L.; Zhu, C.P.; Yao, C.; Yin, C.; Jiang, X.Y. Pseudopotential multi-relaxation-time lattice Boltzmann model for cavitation bubble collapse with high density ratio. *Chin. Phys. B* **2016**, *25*, 104–701. [[CrossRef](#)]
25. Huang, H.; Sukop, M.C.; Lu, X.Y. *Multiphase Lattice Boltzmann Methods: Theory and Application*; John Wiley & Sons: Hoboken, NJ, USA, 2015; pp. 121–122. ISBN 978-1-118-97133-8.
26. Shan, X. Pressure tensor calculation in a class of nonideal gas lattice Boltzmann models. *Phys. Rev. E Stat. Nonlinear Soft Matter Phys.* **2008**, *77*, 06670201–06670206. [[CrossRef](#)] [[PubMed](#)]
27. Yuan, P.; Schaefer, L. Equations of state in a lattice Boltzmann model. *Phys. Fluids* **2006**, *18*, 04210101–04210111. [[CrossRef](#)]
28. Porter, M.L.; Coon, E.T.; Kang, Q.; Moulton, J.D.; Carey, J.W. Multicomponent interparticle-potential lattice Boltzmann model for fluids with large viscosity ratios. *Phys. Rev. E Stat. Nonlinear Soft Matter Phys.* **2012**, *86*, 03670101–03670108. [[CrossRef](#)] [[PubMed](#)]
29. Martys, N.S.; Chen, H. Simulation of multicomponent fluids in complex three-dimensional geometries by the lattice Boltzmann method. *Phys. Rev. E* **1996**, *53*, 743–750. [[CrossRef](#)]
30. Zou, Q.; He, X. On pressure and velocity boundary conditions for the lattice Boltzmann BGK model. *Phys. Fluids* **1997**, *9*, 1591–1598. [[CrossRef](#)]
31. Krüger, T.; Kusumaatmaja, H.; Kuzmin, A.; Shardt, O.; Silva, G.; Viggien, E.M. *The Lattice Boltzmann Method*; Springer: Cham, Switzerland, 2017; pp. 199–200. ISBN 978-3-319-44647-9.
32. Plesset, M.S.; Chapman, R.B. Collapse of an initially spherical vapour cavity in the neighbourhood of a solid boundary. *J. Fluid Mech.* **1971**, *47*, 283–290. [[CrossRef](#)]
33. Bernardin, J.D.; Mudawar, I.; Walsh, C.B.; Franses, E.I. Contact angle temperature dependence for water droplets on practical aluminum surfaces. *Int. J. Heat Mass Transf.* **1997**, *40*, 1017–1033. [[CrossRef](#)]

